Contents

A   Parametrization updates with respect to Willen et al. (2022)

We extended the parametrization of AIS IMC, implemented by the design matrices $X_{\text{AIS-IMC}}^{\text{GRAV}}$ and $X_{\text{AIS-IMC}}^{\text{AIS-ALT}}$, to the peripheral glaciers on surrounding islands, e.g. Berkner Island, Alexander Island, Thurston Island, Siple Island. We use the polygon data set from Mouginot et al. (2017) to define the boundaries of grounded ice. Likewise, we extended the parametrization of FAC, implemented by $X_{\text{AIS-FAC}}^{\text{AIS-ALT}}$ and $X_{\text{AIS-FAC}}^{\text{AIS-FAC}}$, to the peripheral glaciers.

Furthermore, we slightly modified the GIA parametrization in Antarctica, implemented by $X_{\text{GIA}}^{\text{GRAV}}$ and $X_{\text{GIA}}^{\text{AIS-ALT}}$. From our validation experiments, we found that we were not able to retrieve reasonable GIA results for the northern part of the Antarctic Peninsula (Graham Land). We attribute this to the low quality of surface elevation changes derived from radar altimetry here (e.g. Schröder et al., 2019). In turn the significant misfit between GRACE/GRACE-FO products and CryoSat-2 products is captured by an unphysical GIA signal. This is also the case for other inverse GIA estimates (e.g. Gunter et al., 2014; Engels et al., 2018; Willen et al., 2020). To prevent an unphysical GIA, we decided not to co-estimate GIA in this particular region. We did not include local GIA patterns at the Peninsula in our local GIA-pattern parametrization. Instead we approach the GIA effect here by a global GIA model result which is then subtracted from the observations. We model the GIA effect with an ICE-6G ice history that solely exists in the Graham Land Region by using the SELEN[4] (Spada and Melini, 2019). Figure S1 illustrates the modified GIA parametrization with the Antarctic Peninsula GIA pattern in the spatial domain. We admit that this GIA pattern has limitations to represent the true GIA effect in this region. The viscosity structure shown by Ivins et al. (2021) indicates that GIA effects similar to the Amundsen Sea region, in terms of response time scales, can also be expected on the Antarctic Peninsula. This means that this pattern, will only account for the true GIA effect here to some extent and we will not be able to resolve GIA effects that are caused by changes in ice loading over the last centuries here. Nevertheless, we argue that this methodological adjustment allows to, at least, limit the bias to the entire Antarctic GIA estimate. The reader is also referred to the discussion we provide in Sect. 4.

Even by implementing the hydrology parametrization, we still found significant trends in the residuals that we interpret as hydrological signal, in addition to some other less significant signals, e.g. from tectonics. We explain these trends by the limitations of the hydrology parametrization we apply. However, so far there is no sophisticated global hydrology parametrization available and the detection of hydrological signals from GRACE/GRACE-FO is a research topic with a major focus under investigation (Chen et al., 2022). Since our focus here are mass changes in Antarctica, we implement a pragmatic solution to prevent possible bias towards Antarctic mass estimates due to far-field effects by residual hydrological signals. We removed a hydrological residual fingerprint from the GRACE/GRACE-FO data. This fingerprint is generated from residuals from an initial inversion run. First, we apply a de-stripe filter and Gaussian filter (halfresponse: 250 km) to

surface density rate in kg m^{-2}a^{-1}
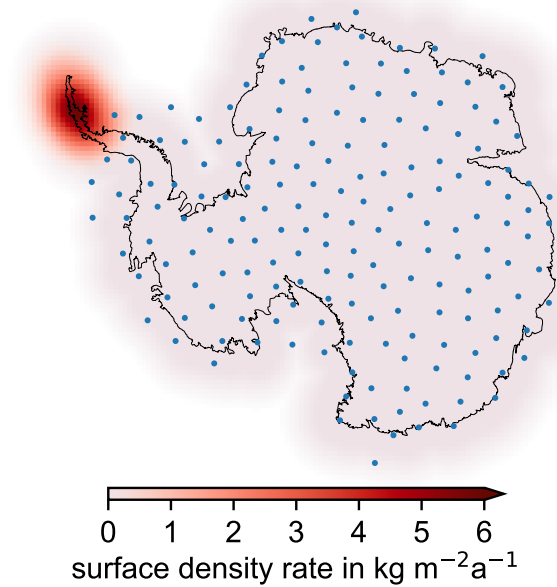
Figure S1: The adapted Antarctic GIA parametrization: Antarctic GIA parameters are global patterns from local deglaciation impulses according to Willen et al. (2022). Blue dots: centres of deglaciation impulses. Due to altimetry quality limitations on the Antarctic Peninsula (Graham Land), GIA is not co-estimated in this particular region. Instead we accounted for the GIA effect here by implementing a GIA fingerprint from a tailored ice history modelled with SELEN[4] (Spada and Melini, 2019). The spatial pattern of the GIA-related surface density change of this Antarctic Peninsula fingerprint is illustrated over the Antarctic continent.

kg m^{-2} a^{-1}
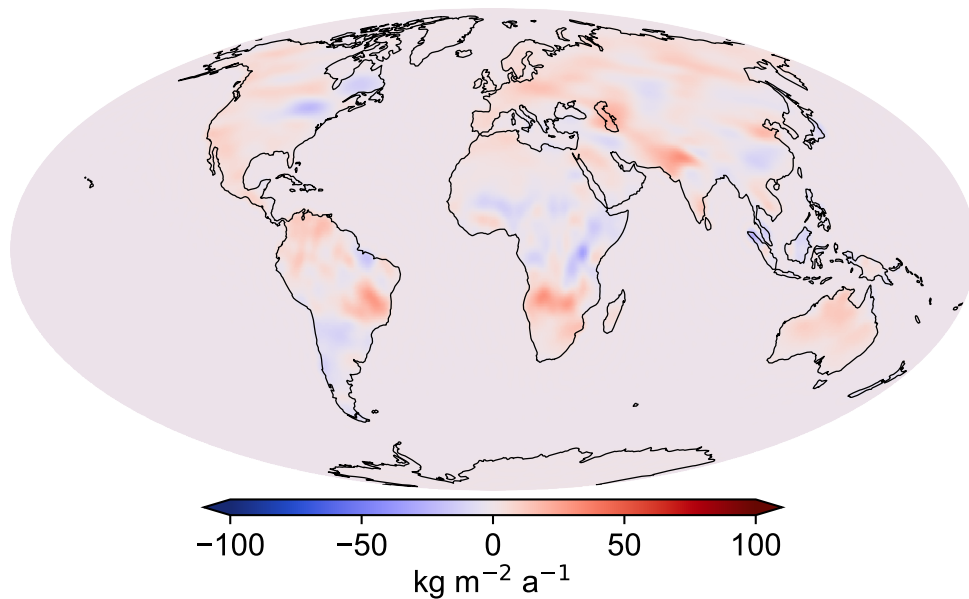
Figure S2: The hydrological residual fingerprint implemented as an additional hydrological parameter to prevent bias on mass changes in Antarctica due to hydrological far field effects which are not accounted for by the used hydrology parameters. The fingerprint is derived from initial inversion results.

GRACE/GRACE-FO residuals. Second, we cut out the residual signal over the continents excluding Greenland and Antarctica. Third, we assume this residual signal as a purely hydrological signal on the continents and calculate its sea level fingerprint by solving the sea level equation (Clarke et al., 2005). Lastly, this hydrological residual fingerprint (Fig. S2) is introduced as an additional parameter.

B Variance Component Estimation (VCE)

Initially, we have solved the generalized least squares adjustment (cf. Eq. (12) in Willen et al. (2022)):

$$\boldsymbol{N} = \boldsymbol{X}^{\mathrm{T}} \boldsymbol{P} \boldsymbol{X} \tag{S1}$$

$$\boldsymbol{n} = \boldsymbol{X}^{\mathrm{T}} \boldsymbol{P} \boldsymbol{d} \tag{S2}$$

$$\hat{\boldsymbol{\beta}} = \boldsymbol{N}^{-1} \boldsymbol{n} \qquad \text{and} \qquad C(\hat{\boldsymbol{\beta}}) = \sigma^2 \boldsymbol{N}^{-1}. \tag{S3}$$

To optimize the estimation of the parameters, $\hat{\boldsymbol{\beta}}$, we introduce a relative weighting of the uncertainty information of each observational group. To do so, we apply a variance component estimation (VCE) and iteratively determine variance components for the gravimetry, altimetry, and FAC input data sets. The theoretical background of VCE is extensively documented elsewhere, e.g. Koch (1999). To simplify the notation, the weight matrix, $\boldsymbol{P}$, incorporates the error-covariance information, e.g. derived from uncertainty propagation or stochastic error characterization (Willen et al., 2022), and the relative weights of the uncertainty information of the three observational groups determined by VCE.

The VCE leads to relative downweighting of altimetry observations and input FAC changes with respect to gravimetry observations. The estimated variance factors, $(\hat{\sigma}_0^{\mathrm{GRAV}})^2$, $(\hat{\sigma}_0^{\mathrm{AIS\text{-}ALT}})^2$, and $(\hat{\sigma}_0^{\mathrm{AIS\text{-}FAC}})^2$, are 3, 35, and 19, respectively.

C Tikhonov regularization

The simulation experiments by Willen et al. (2022) demonstrated the benefit from including the full error-covariance information in the parameter estimation, if correlated errors are present. In particular, ignoring correlated errors leads to a low signal-to-noise ratio of the Antarctic GIA result. However, the experiments according to Willen et al. (2022) assumed to have full knowledge of the error-covariance information, which is an important idealization of the true problem.

Preliminary results, however, indicated artificial and unphysical GIA-induced effects unsupported by GNSS measurements and GIA models. Notable is a large GIA-induced uplift in the Transantarctic Mountains where there is no evidence from independent data. After extensive testing, we conclude that the assumed information on spatial error correlations from Willen et al. (2022), implemented in $\boldsymbol{P}$, are insufficient to account for the true error correlations and may even lead to unphysical results during the parameter estimation. This holds for each observational group individually. Figure S6d–f provides spatial maps of these preliminary results. We provide in Sect. 4 further discussion on error covariances

Nevertheless, the simulation experiments from Willen et al. (2022) demonstrated that spatially correlated errors need to be accounted for. We approach the limited error covariance information by implementing a Tikhonov regularization (Tikhonov et al., 1995) by adding a regularization matrix, $\boldsymbol{\Psi}$, to the normal equation matrix, $\boldsymbol{N}$ (Eq. 3, S1). $\boldsymbol{\Psi}$ is designed to regularize, i.e. to damp, the Antarctic GIA parameters, $\boldsymbol{\beta}_{\mathrm{GIA,ANT}}$, only. $\boldsymbol{\Psi}$ is a
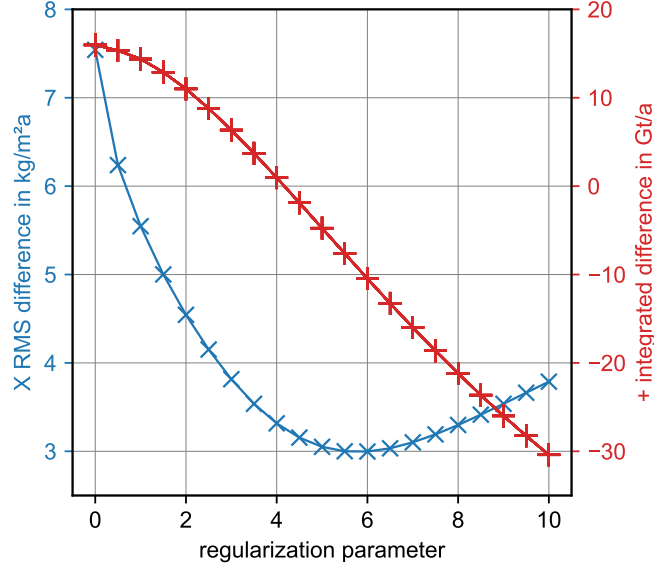
Figure S3: Antarctic GIA integral results of simulation experiments adapting Experiment 2 in Willen et al. (2022). This experiment includes regularization of Antarctic GIA parameters (Eq. 3) while neglecting for correlated errors in the input data. The deviation of the estimated GIA from the original GIA is shown in terms of RMS error (x,blue) and in terms of integrated GIA mass effect (+,red) for regularization parameters, ε, ranging from 0 to 10. For $\varepsilon = 4.17$ the integrated difference is close to zero. Note that this optimum only holds for the simulation experiment and cannot be applied to the real data case. The reader is referred to Willen et al. (2022) for further details on the simulation set up.

square matrix with the two dimensions equal to the total amount of parameters. The non-zero elements are

$$\psi_{ij} = \varepsilon \delta_{ij}, \qquad i, j = 1, ..., N_{\text{GIA}}. \tag{S4}$$

N_{GIA} is the number of Antarctic GIA parameters, ε is the regularization parameter, and δ_{ij} is the Kronecker delta.

C.1 Simulation experiments justifying the regularization

To test whether we get meaningful results using this regularization—when we neglect for spatially correlated errors within the parameter estimation—we have performed simulation experiments analogous to Willen et al. (2022). We can find a regularization factor such that the error of the integrated GIA mass effect in Antarctica is close to zero (Fig. S3). The simulation results where this regularization factor is applied (Fig. S3 and S4) demonstrate that we can reproduce Antarctic GIA with only a slightly higher RMS error than if we would have full knowledge of the error covariance information ($3.3\,\text{kg}\,\text{m}^2\text{a}^{-1}$ vs. $2.8\,\text{kg}\,\text{m}^2\text{a}^{-1}$). In general the RMS errors are higher compared to utilizing the full error covariance information, in particular in case of IMC ($7.3\,\text{kg}\,\text{m}^2\text{a}^{-1}$ vs. $2.3\,\text{kg}\,\text{m}^2\text{a}^{-1}$). We conclude from the simulation experiments that the regularization prevents overfitting and reduces the sensitivity of the GIA result against spatially correlated errors of the data sets. But the regularization is less capable to suppress correlated errors than the full knowledge of the error-covariance information.
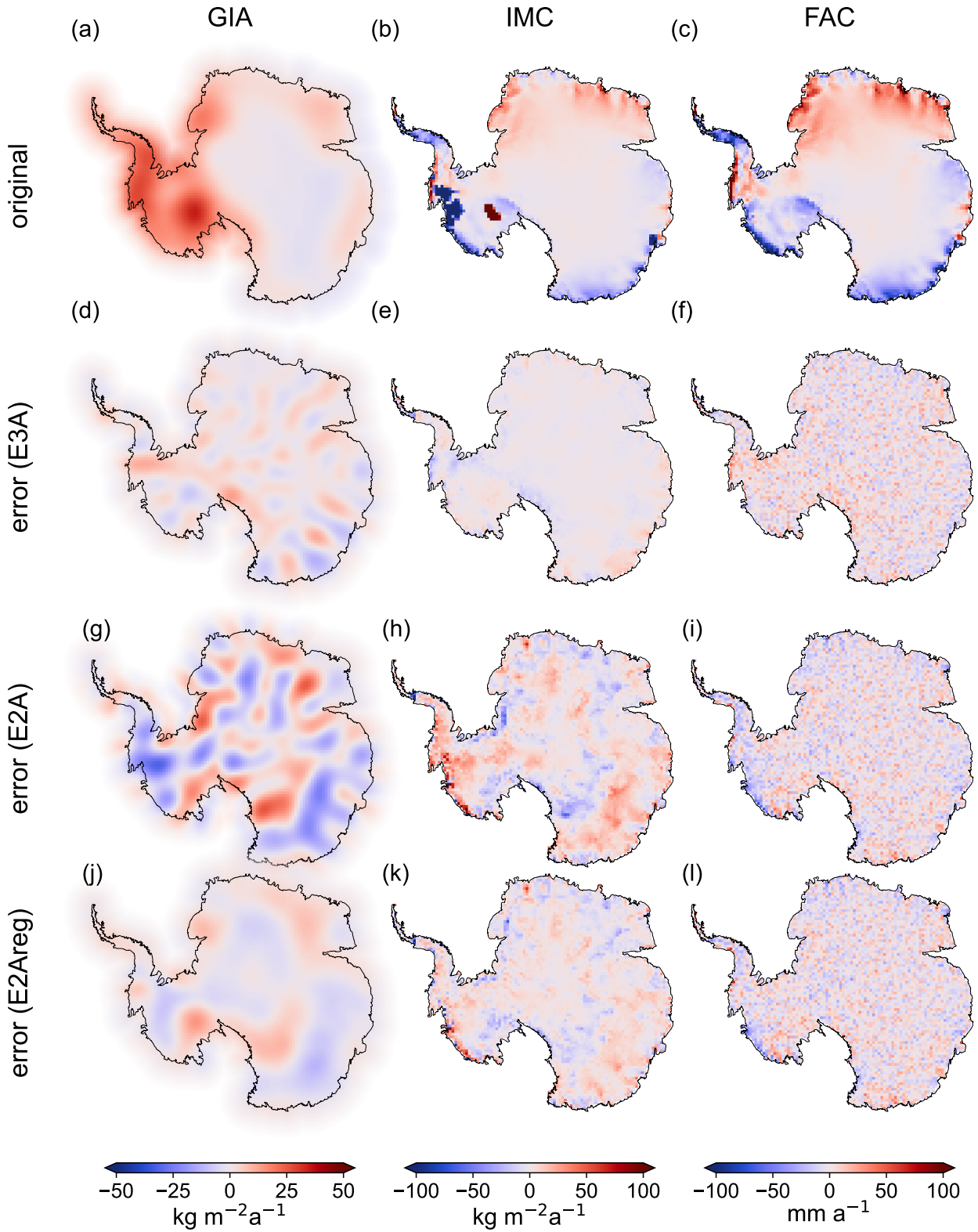
Figure S4: Antarctic maps of results from simulation experiments according to Willen et al. (2022). With the simulation experiments we test the ability of the inversion framework to resolve the glacial isostatic adjustment (GIA) signal (a), the ice mass change (IMC) signal (b), and the firn air content (FAC) change signal (c). The errors of the estimates are shown in (d–l) from three different experiments. In Experiment 3A (E3A) we assumed full knowledge of error covariance information and account for it in the estimation (d–f). The RMS differences from the original signals are $2.8 \, \text{kg m}^2\text{a}^{-1}$, $2.3 \, \text{kg m}^2\text{a}^{-1}$, and $10.8 \, \text{mm a}^{-1}$ in case of GIA, IMC, and FAC, respectively. The integrated differences are $7.6 \, \text{Gt a}^{-1}$, $-8.9 \, \text{Gt a}^{-1}$, and $6.9 \, \text{km}^3\text{a}^{-1}$, respectively. In Experiment 2A (E2A) we completely neglect for correlated errors within the inversion while they are present in the simulated observations (g–i). The RMS differences are $7.4 \, \text{kg m}^2\text{a}^{-1}$, $8.6 \, \text{kg m}^2\text{a}^{-1}$, and $12.3 \, \text{mm a}^{-1}$; integrated differences are $-16.7 \, \text{Gt a}^{-1}$, $22.5 \, \text{Gt a}^{-1}$, and $-15.3 \, \text{km}^3\text{a}^{-1}$. Experiment 2A with regularization (E2Areg) equals E2A but we applied a regularization using a regularization factor of $\varepsilon = 4.17$ (j–l) (cf. Figure S3). The RMS differences are $3.3 \, \text{kg m}^2\text{a}^{-1}$, $7.3 \, \text{kg m}^2\text{a}^{-1}$, and $12.1 \, \text{mm a}^{-1}$; integrated differences are $0.0 \, \text{Gt a}^{-1}$, $2.2 \, \text{Gt a}^{-1}$, and $-9.2 \, \text{km}^3\text{a}^{-1}$.

C.2 Choice of the regularization parameter
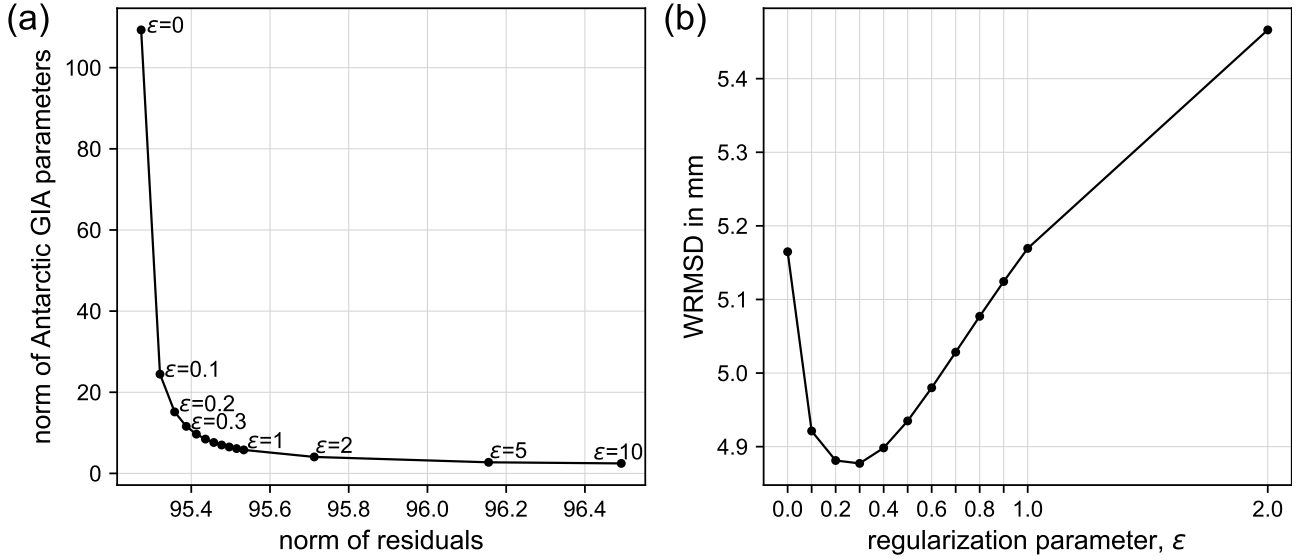
Figure S5: (a) The L-curve illustrates the trade-off between the norm of residuals and the norm of estimated Antarctic GIA parameters depending on the regularization factor ε. (b) The WRMSD values (Eq. 4) depending on the regularization parameter. The WRMSD is a measure of the difference between the Antarctic GIA inversion result and the independent GNSS data.

For the real-data application, we first determine a weight matrix $\tilde{\boldsymbol{P}}$, which solely accounts for uncorrelated errors (Sect. 2.2), i.e. the diagonal elements of $\boldsymbol{P}$. Note that we also ignore spatially correlated errors when determining the variance components of the observation groups. Second, we chose the regularization factor according to a trade-off between minimizing the norm of the uncertainty-weighted residuals, $\|\tilde{\boldsymbol{e}}\|_2 = \sqrt{\boldsymbol{e}^{\mathrm{T}} \tilde{\boldsymbol{P}} \boldsymbol{e}}$, and minimizing the norm of the parameters, $\|\boldsymbol{\beta}_{\mathrm{GIA,ANT}}\|_2$. This trade-off between a best-fit solution and a short solution vector, i.e. a simple solution in terms of Occam's razor, is determined using the L-curve criterion (Hansen, 2001).

Figure S5 illustrates the relation between the norm of residuals and the norm of parameters in dependence on the regularization parameter. Based on the L-curve test (Figure S5a), a regularization parameter of $\varepsilon = 0.3$ or 0.4 may be used to choose a preferred inversion solution. In general the impact on the norm of residuals by regularizing Antarctic GIA is rather small, as Antarctic GIA is only one part of global mass changes. To further substantiate the choice of the regularization parameter, we compare the Antarctic GIA results of each regularization parameter to the independent GNSS data (Sect. 2.3). In agreement with the L-curve, we found a minimum WRMSD between the GNSS-derived bedrock motion and the GIA inversion result using $\varepsilon = 0.3$ (Figure S5b). We choose the inversion result based on $\varepsilon = 0.3$ as the *preferred inversion solution.*

Note that using the error covariance information from Willen et al. (2022) and applying a regularization leads to unphysical results (Fig. S6g–i). This is also the case if the error-covariance information of each individual observation group is incorporated separately in the parameter estimation.
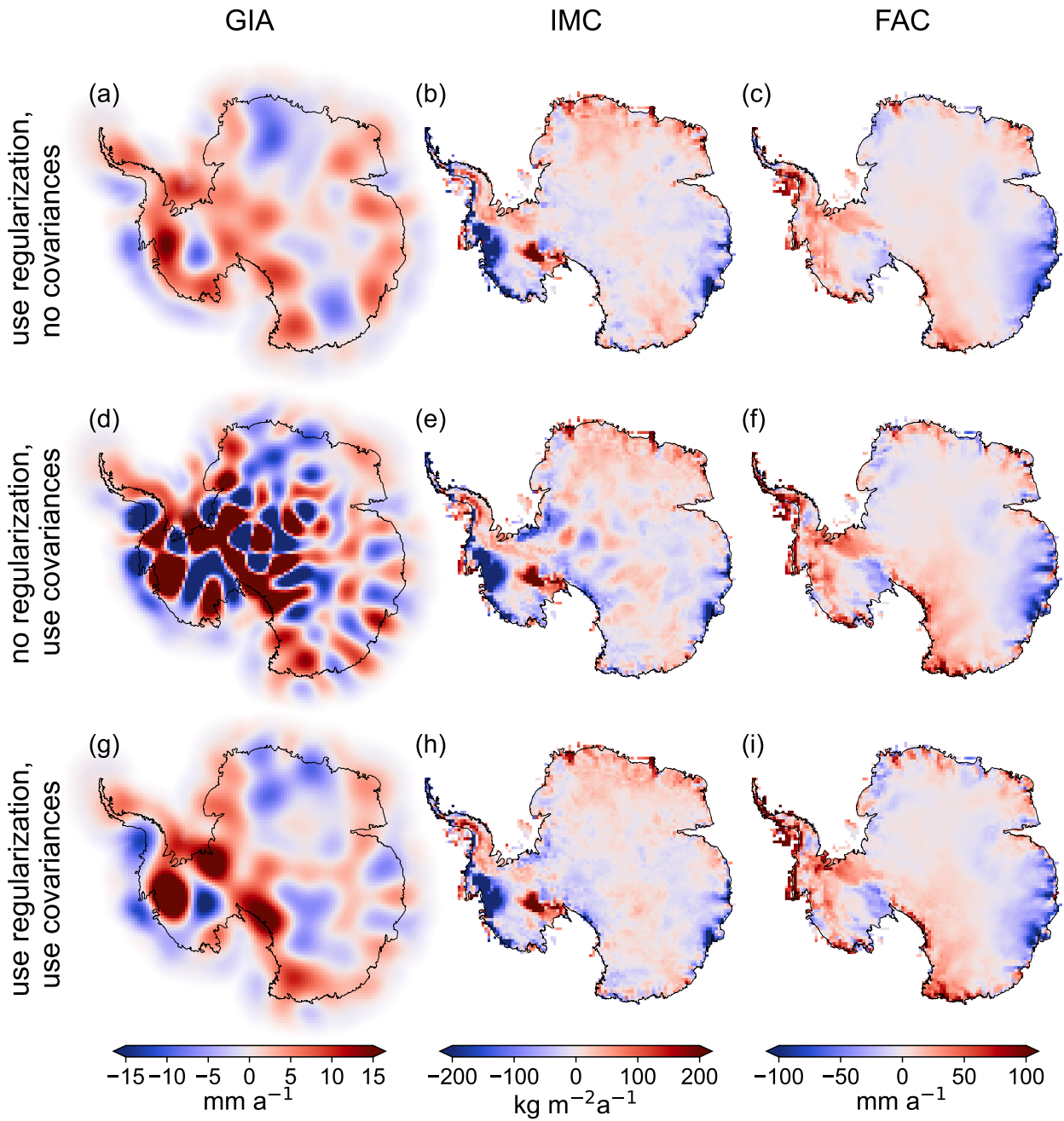
Figure S6: (a–c) The results from the preferred inversion solution as shown in Fig. 3, i.e. correlated errors are not accounted for in the parameter estimation and Antarctic GIA parameters are regularized. (d–f) The results from an inversion solution where the error-covariance information is used within the parameter estimation and no regularization is applied. (g–i) The results from an inversion solution where the error-covariance information is used within the parameter estimation and the same regularization is applied as in preferred inversion solution as described in Sect. C.
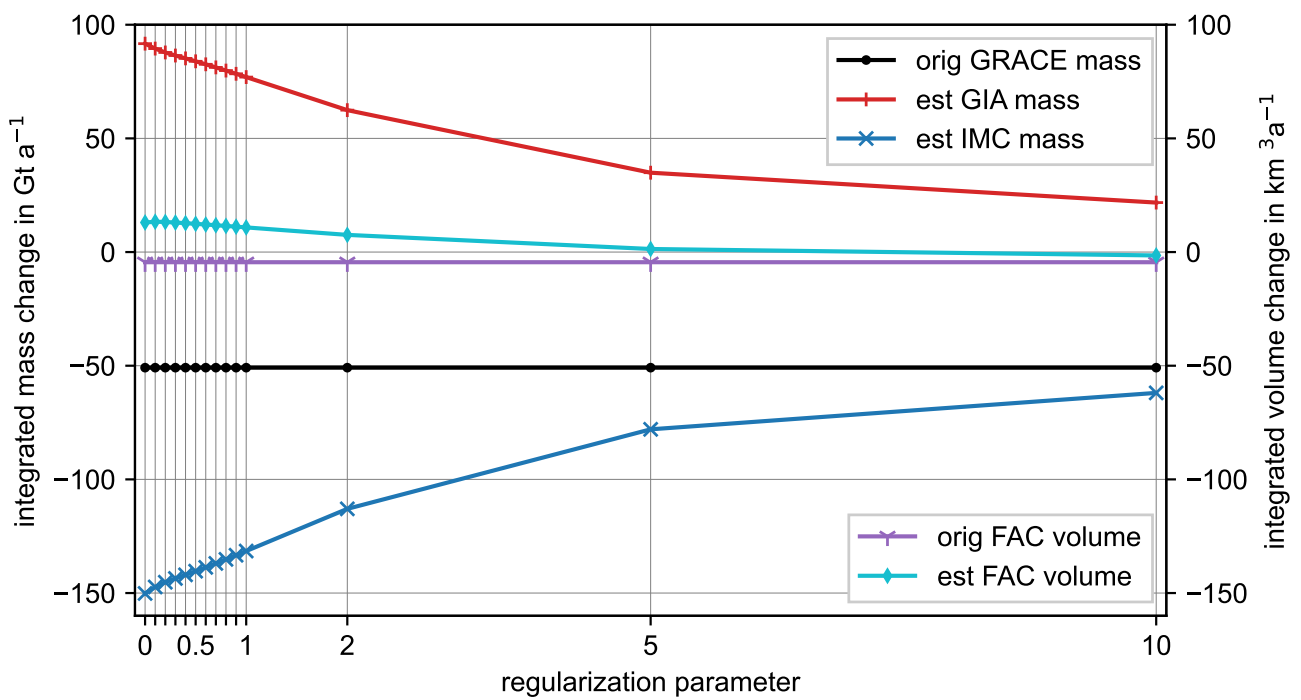
Figure S7: Integrated values for estimated ice mass change (IMC, ⊠, blue), glacial isostatic adjustment (GIA) mass effect (+, red), and volume change of firn air content (FAC, ◇, cyan), depending on the chosen regularization parameter. Modelled FAC volume change (Y, purple) and observed mass changes from GRACE/GRACE-FO (., black) are shown for comparison.

D   Supplemental figures
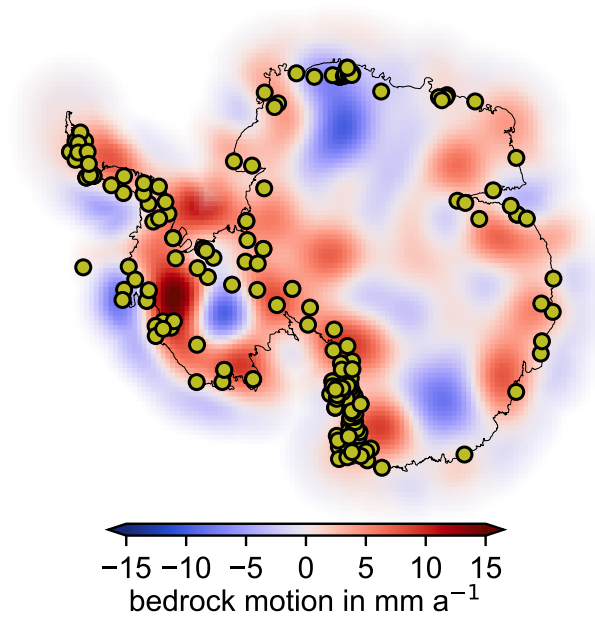
Figure S8: Antarctic GIA bedrock motion result from the preferred inversion solution. The location of GNSS sites are indicated with yellow circles where bedrock motion data according to Buchta et al. (2022) for comparison is available.
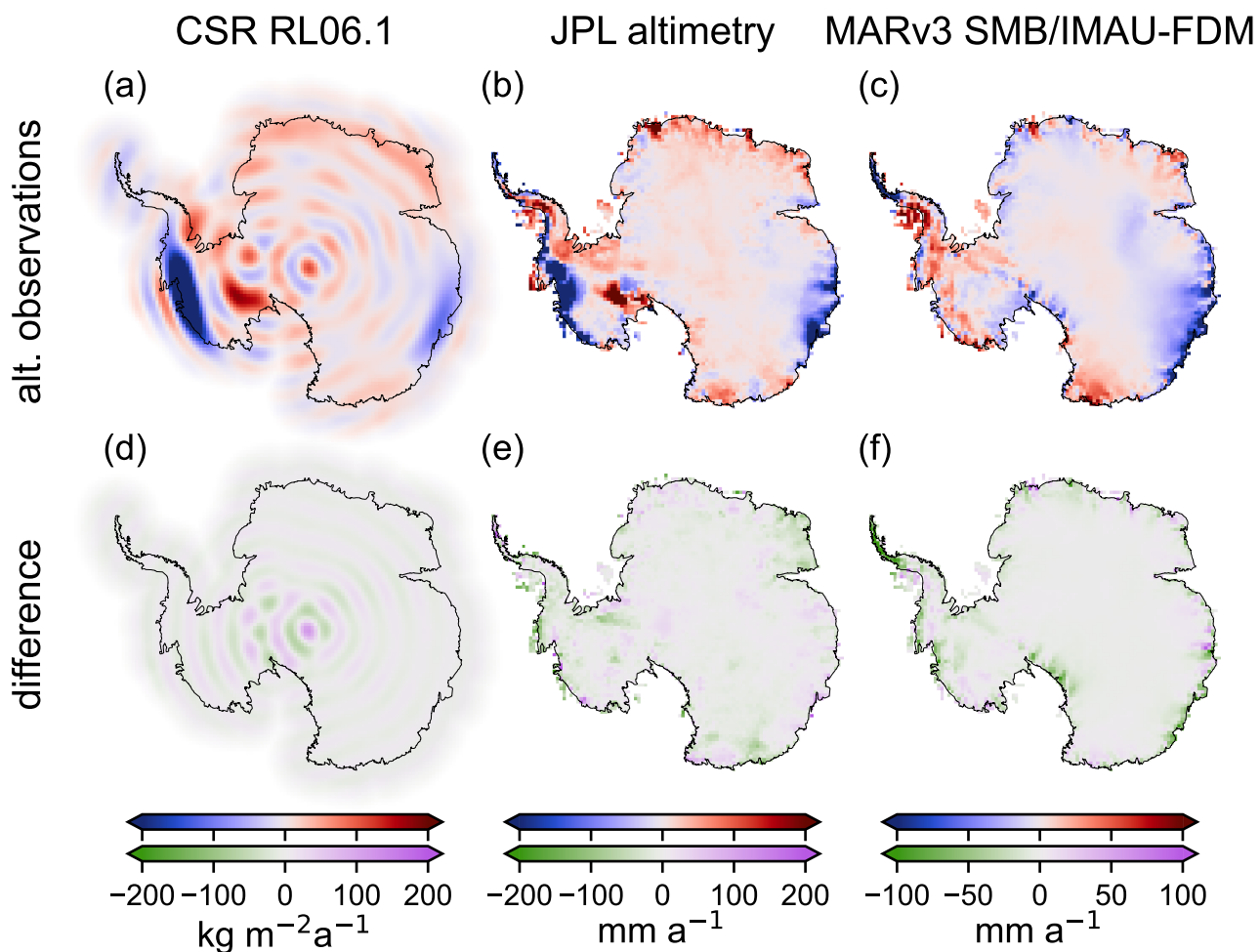
Figure S9: Antarctic maps of alternative input data sets used in the sensitivity tests (a–c) and their difference to the data sets used for the preferred inversion solution (d–f). a) The surface density rate from CSR RL06.1 GRACE/GRACE-FO products (Pie et al., 2021) and d) its difference to the ITSG-Grace2018 product (Mayer-Gürr et al., 2018). A decorrelation filter (Swenson and Wahr, 2006) is applied to suppress error stripe patterns. b) Surface elevation trend from Nilsson et al. (2022) and e) its difference to the CryoSat-2-derived rate updated according to Helm et al. (2014). c) FAC based on the cumulated SMB anomaly trend derived from MARv3.11 SMB (Kittel et al., 2021) and IMAU-FDM and f) its difference to FAC based on RACMO2.3p2 SMB (Wessem et al., 2018) and IMAU-FDM.
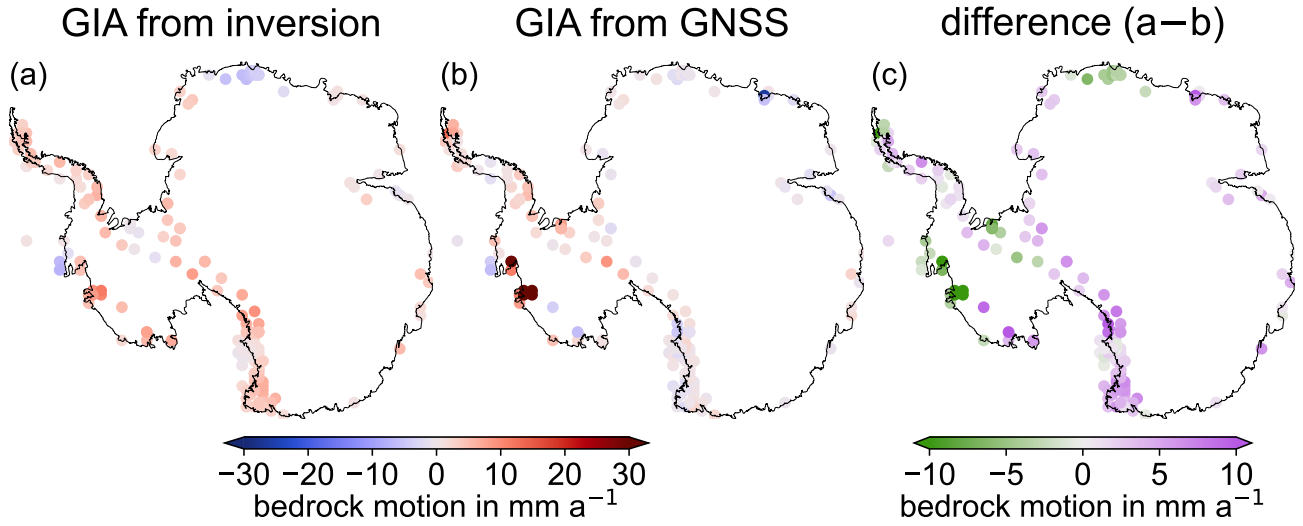
Figure S10: Comparison of GIA-related bedrock motion at GNSS sites from the preferred inversion solution (a), from GNSS observations (b), and the difference between both (c).
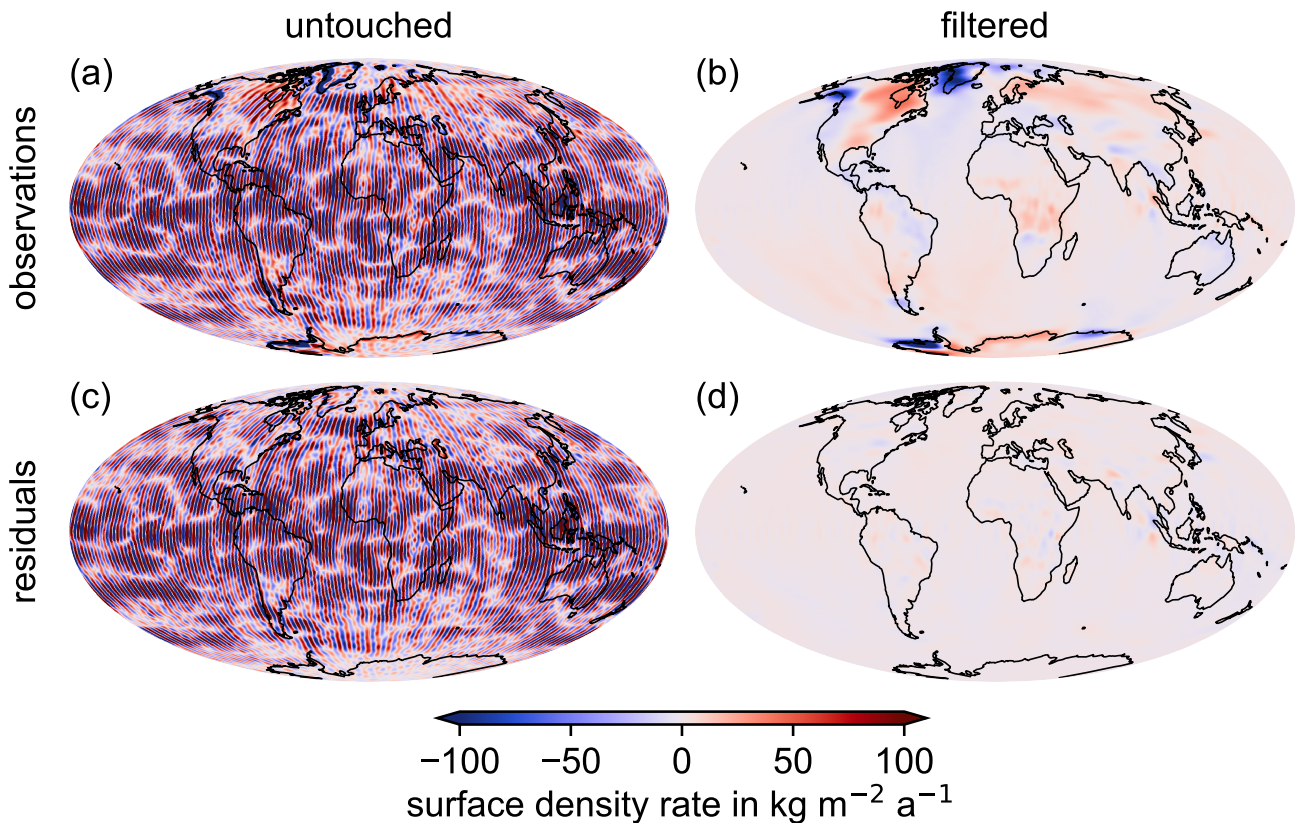
Figure S11: Global maps of observations and residuals of GRACE/GRACE-FO surface density rate in the spatial domain. a) GRACE/GRACE-FO-derived mean rate, i.e. the inversion input data illustrated in the spatial domain, b) GRACE/GRACE-FO data where noise patterns are reduced using a decorrelation filter (Swenson and Wahr, 2006) and 250 km Gaussian smoothing, c) the GRACE/GRACE-FO residuals of the preferred inversion solution illustrated in the spatial domain. d) the GRACE/GRACE-FO residuals with the same filter applied as in (b). The smoothing filter is applied for visualization purposes only and not part of the parameter estimation.
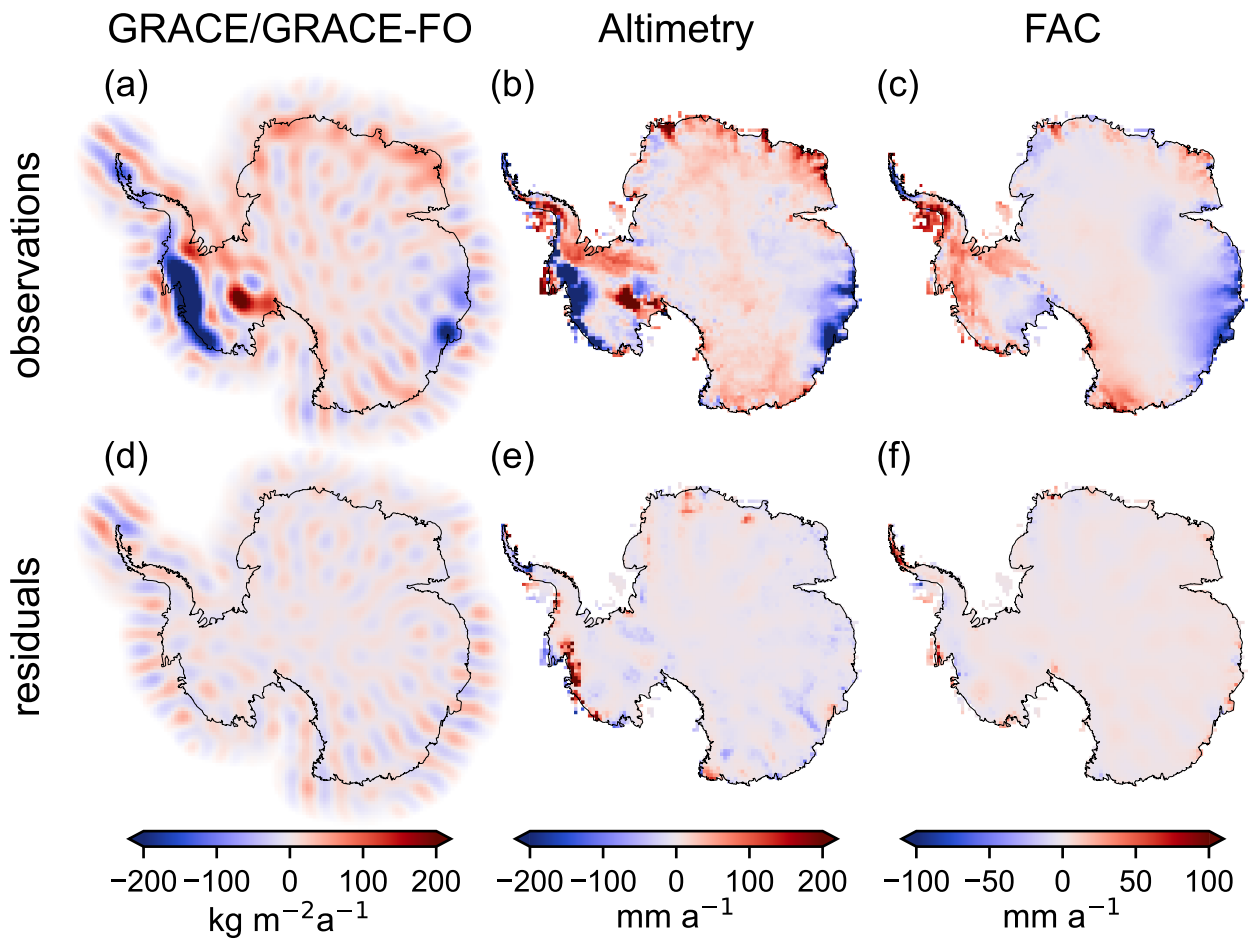
Figure S12: Antarctic maps of observations (a–c) and residuals of the preferred inversion solution (d–f). a) GRACE/GRACE-FO surface density rate and d) residual rate similar to Fig. S11a+c). b) CryoSat-2 derived surface elevation rate and e) the residual surface elevation rate. c) FAC rate and f) FAC residual rate.
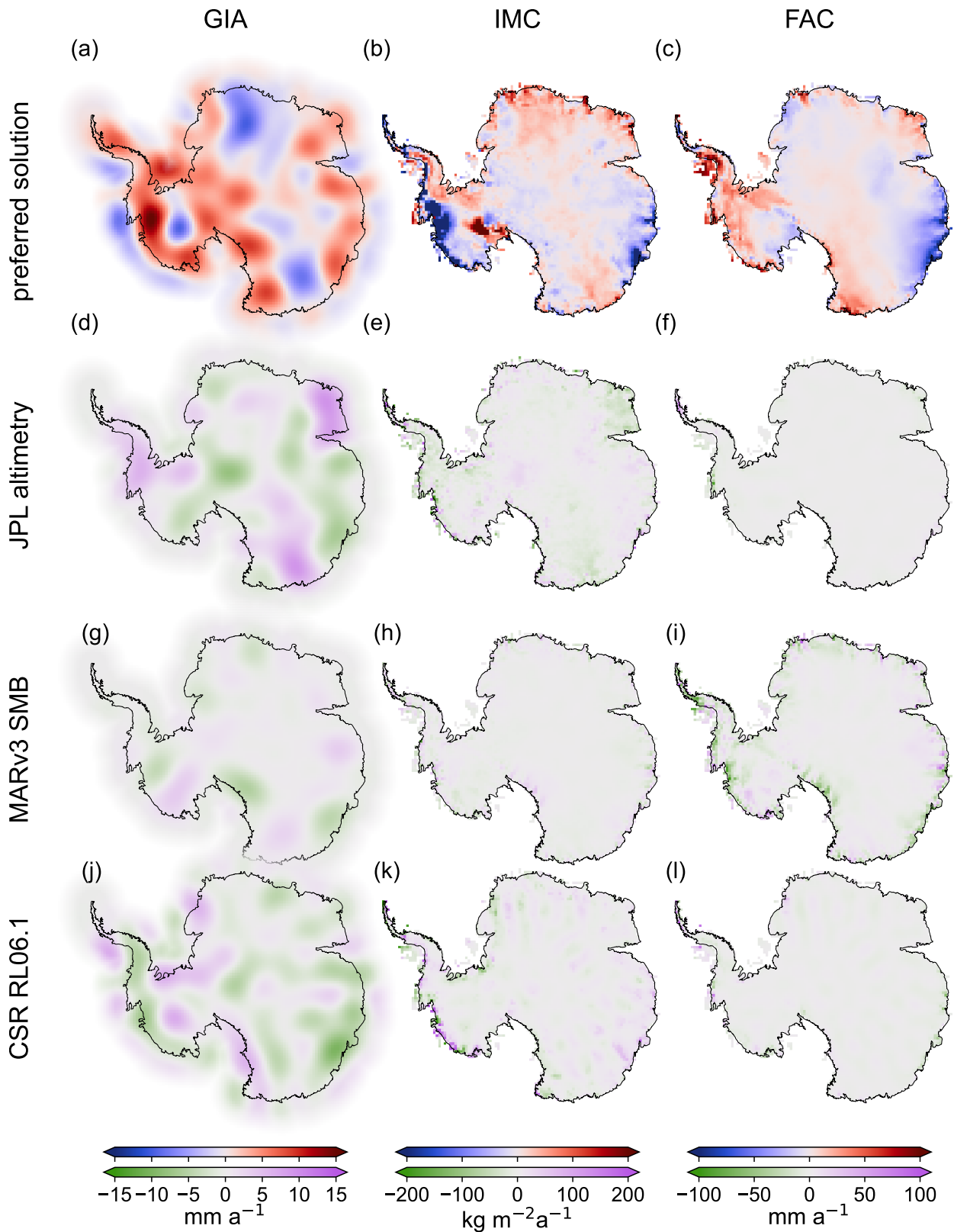
Figure S13: Results from sensitivity tests using alternative input data sets (Fig. S9). The first row (a–c) shows the results from the preferred inversion result (Fig. 3). The second row (d–f) shows the differences between the inversion results and the first row where the surface elevation rate from (Nilsson et al., 2022, Fig. S9a) is used (test result minus preferred inversion solution). Similar, the third row (g–i) and fourth row (j–l) shows differences to the inversion results with MARv3.11 SMB data (Kittel et al., 2021, Fig. S9b) and CSR RL06.1 gravitational fields (Pie et al., 2021, Fig. S9c), respectively.
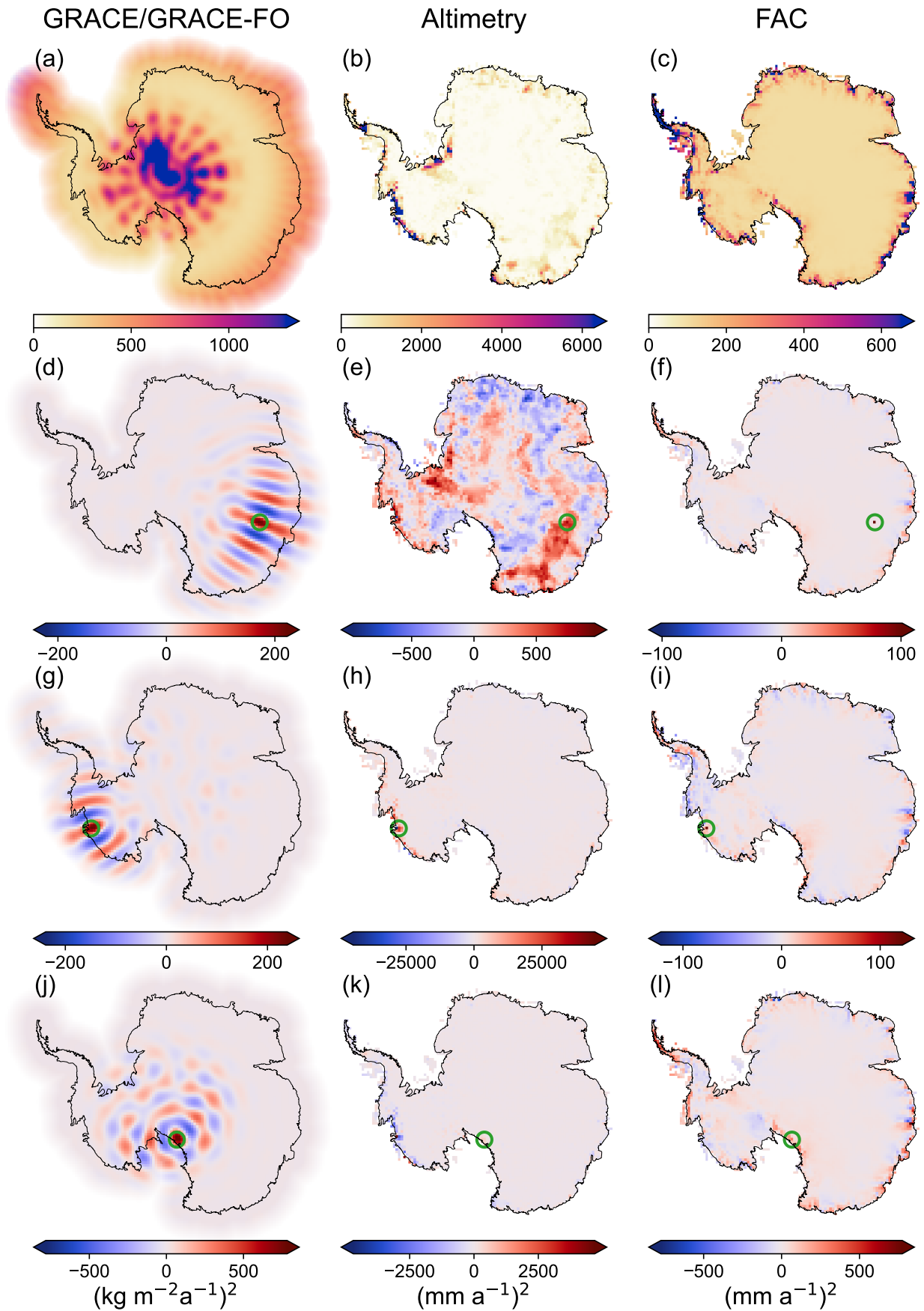
Figure S14: Maps illustrate the variances (a–c) and covariances (d–l) of the input data sets, column by column indicated by the headline for satellite gravimetry (GRACE/GRACE-FO), altimetry, and firn air content (FAC). Covariances are shown for a grid cell highlighted with a green circle in Wilkes Land (d–f), Amundsen Sea Embayment (g–i), and Transantarctic Mountains (j–l). The co-/variance information (Eq. 2) is propagated to the Antarctic grid for illustration purposes only.
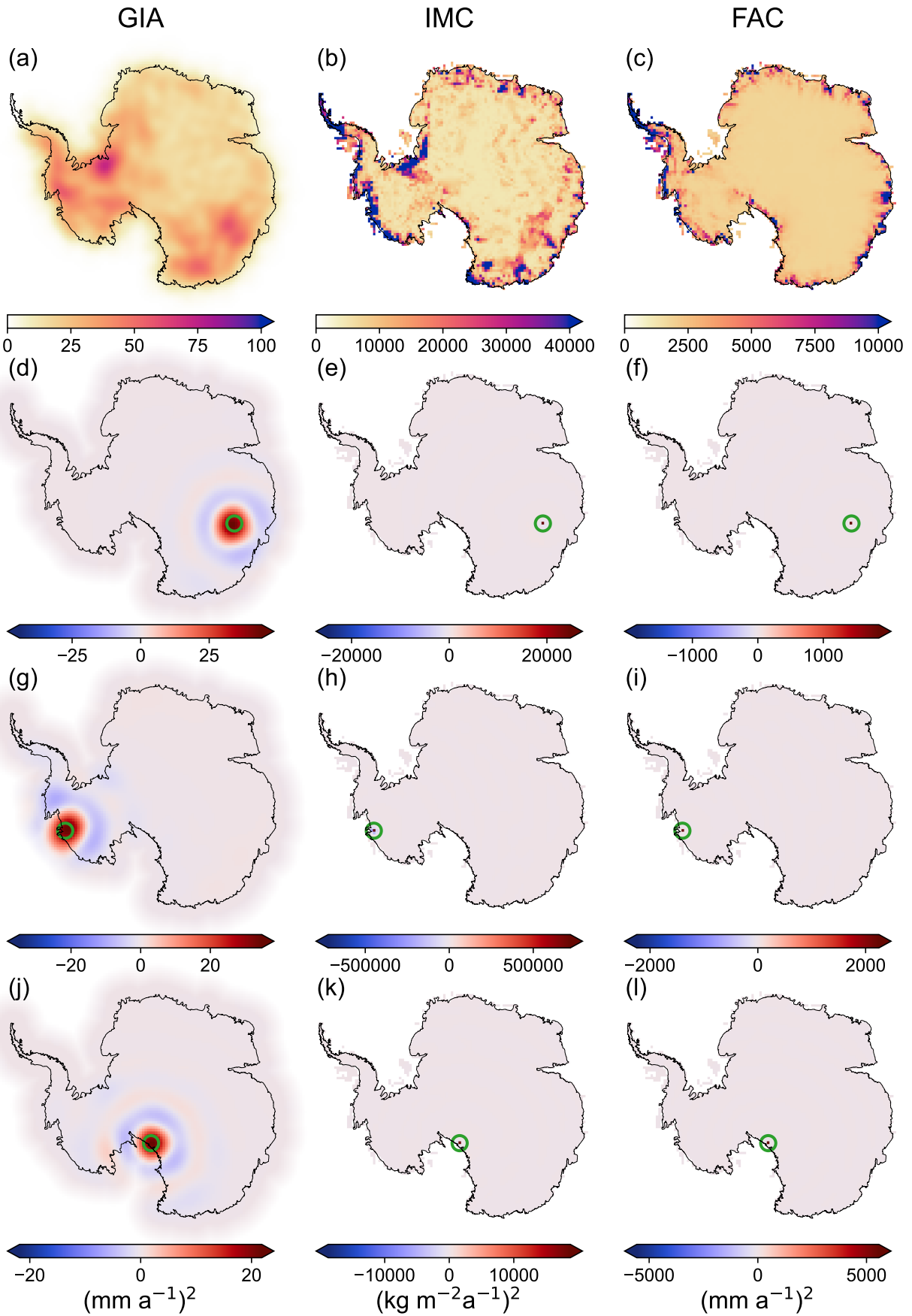
Figure S15: Similar to Fig. S14, maps illustrate the variances (a–c) and covariances (d–l) of the estimated parameters (Eq. 3), column by column for each parameter type indicated by the headline: GIA, Antarctic ice mass change (IMC), change of firn air content (FAC). The example points are the same as shown in Fig. S14.
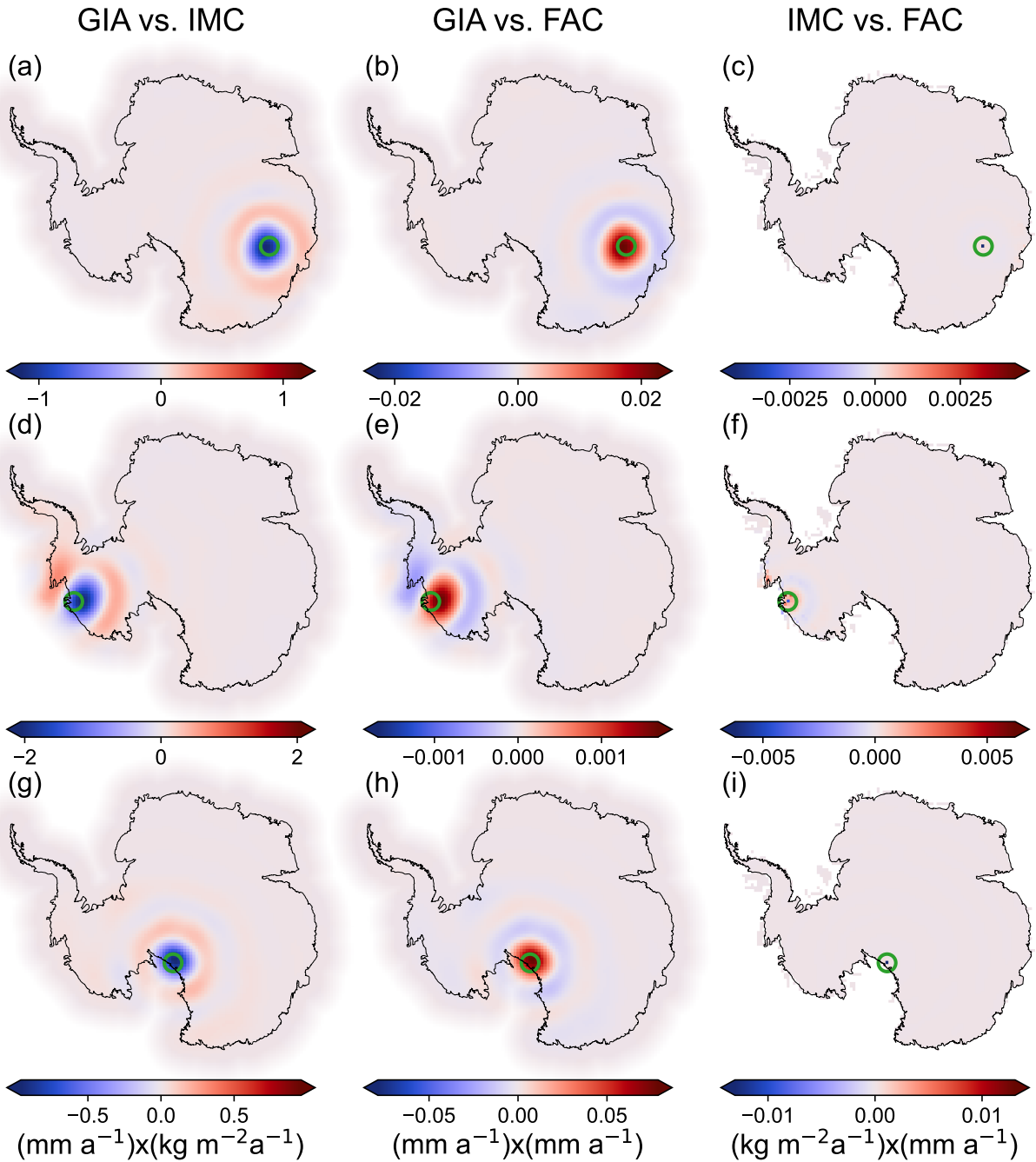
Figure S16: Maps illustrate the covariance for the example points in Fig. S14 and S15 between the parameter types column by column indicated in the headline: GIA, Antarctic ice mass change (IMC) and change of firn air content (FAC).

References

Buchta, E., M. Scheinert, M. King, T. Wilson, E. Kendrick, A. Koulali, P. Clarke, and C. Knöfel (2022). "GIANT-REGAIN: A comprehensive analysis of geodetic GNSS recordings in Antarctica for geodetic and geodynamic applications". In: *SCAR Open Science Conference 2022 - Abstract Book*. SCAR, p. 347. ISBN: 978-0-948277-64-1. URL: https://scar.org/library/conferences/scar-open-science-conferences/abstracts/5876-scar-open-science-conference-2022-abstracts/file.

Chen, J.L., A. Cazenave, C. Dahle, W. Llovel, I. Panet, J. Pfeffer, and L. Moreira (2022). "Applications and Challenges of GRACE and GRACE Follow-On Satellite Gravimetry". In: *Surv. Geophys.*, 41 pp. ISSN: 0169-3298. DOI: 10.1007/s10712-021-09685-x.

Clarke, P.J., D.A. Lavallée, G. Blewitt, T.M. van Dam, and J.M. Wahr (2005). "Effect of gravitational consistency and mass conservation on seasonal surface mass loading models". In: *Geophys. Res. Lett.* 32, p. L08306. DOI: 10.1029/2005GL022441.

Engels, O., B. Gunter, R.E.M. Riva, and R. Klees (2018). "Separating Geophysical Signals Using GRACE and High-Resolution Data: A Case Study in Antarctica". In: *Geophys. Res. Lett.* 45.22, pp. 12, 340–12, 349. ISSN: 0094-8276. DOI: 10.1029/2018GL079670.

Gunter, B.C., O. Didova, R.E.M. Riva, S.R.M. Ligtenberg, J.T.M. Lenaerts, M.A. King, M.R. van den Broeke, and T. Urban (2014). "Empirical estimation of present-day Antarctic glacial isostatic adjustment and ice mass change". In: *The Cryosphere* 8.2, pp. 743–760. ISSN: 1994-0424. DOI: 10.5194/tc-8-743-2014.

Hansen, P. C. (2001). "Computational Inverse Problems in Electrocardiology". In: vol. 4. WIT Press. Chap. The L-curve and its use in the numerical treatment of inverse problems.

Helm, V., A. Humbert, and H. Miller (2014). "Elevation and elevation change of Greenland and Antarctica derived from CryoSat-2". In: *The Cryosphere* 8.4, pp. 1539–1559. ISSN: 1994-0424. DOI: 10.5194/tc-8-1539-2014.

Ivins, E.R., W. van der Wal, D.A. Wiens, A.J. Lloyd, and L. Caron (2021). "Antarctic upper mantle rheology". In: *Geological Society, London, Memoirs* 56, pp. M56–2020. DOI: 10.1144/M56-2020-19.

Kittel, C., C. Amory, C. Agosta, N.C. Jourdain, S. Hofer, A. Delhasse, S. Doutreloup, P.-V. Huot, C. Lang, T. Fichefet, and X. Fettweis (2021). "Diverging future surface mass balance between the Antarctic ice shelves and grounded ice sheet". In: *The Cryosphere* 15.3, pp. 1215–1236. DOI: 10.5194/tc-15-1215-2021.

Koch, K.R. (1999). *Parameter Estimation and Hypothesis Testing in Linear Models*. 2nd. Springer, Berlin, Heidelberg. ISBN: 978-3-662-03976-2. DOI: 10.1007/978-3-662-03976-2. URL: https://link.springer.com/book/10.1007/978-3-662-03976-2.

Mayer-Gürr, T., S. Behzadpur, M. Ellmer, A. Kvas, B. Klinger, S. Strasser, and N. Zehentner (2018). "ITSG-Grace2018 – Monthly, Daily and Static Gravity Field Solutions from GRACE". In: *GFZ Data Services*. DOI: http://doi.org/10.5880/ICGEM.2018.003.

Mouginot, J., B. Scheuchl, and E. Rignot (2017). *MEaSUREs Antarctic Boundaries for IPY 2007-2009 from Satellite Radar, Version 2*. DOI: 10.5067/AXE4121732AD.

Nilsson, J., A.S. Gardner, and F.S. Paolo (2022). "Elevation change of the Antarctic Ice Sheet: 1985 to 2020". In: *Earth System Science Data* 14.8, pp. 3573–3598. ISSN: 1866-3516. DOI: 10.5194/essd-14-3573-2022.

Pie, N., S.V. Bettadpur, M. Tamisiea, B. Krichman, H. Save, S. Poole, P. Nagel, Z. Kang, G. Jacob, M. Ellmer, E. Fahnestock, F.W. Landerer, C. McCullough, D.-N. Yuan, and D.N. Wiese (2021). "Time Variable Earth Gravity Field Models From the First Spaceborne Laser Ranging Interferometer". In: *J. Geophys. Res. Solid Earth* 126.12, e2021JB022392. ISSN: 2169-9313. DOI: 10.1029/2021JB022392.

Schröder, L., M. Horwath, R. Dietrich, V. Helm, M.R. van den Broeke, and S.R.M. Ligtenberg (2019). "Four decades of Antarctic surface elevation changes from multi-mission satellite altimetry". In: *The Cryosphere* 13.2, pp. 427–449. ISSN: 1994-0424. DOI: 10.5194/tc-13-427-2019.

Spada, G. and D. Melini (2019). "SELEN[4] (SELEN version 4.0): a Fortran program for solving the gravitationally and topographically self-consistent sea-level equation in glacial isostatic adjustment modeling". In: *Geoscientific Model Development* 12.12, pp. 5055–5075. ISSN: 1991-9603. DOI: 10.5194/gmd-12-5055-2019.

Swenson, S. and J. Wahr (2006). "Post-processing removal of correlated errors in GRACE data". In: *Geophys. Res. Lett.* 33, p. L08402. DOI: 10.1029/2005GL025285.

Tikhonov, A. N., A. V. Goncharsky, V. V. Stepanov, and A. G. Yagola (1995). *Numerical Methods for the Solution of Ill-Posed Problems*. Kluwer Academic Publishers. ISBN: 978-90-481-4583-6. DOI: 10.1007/978-94-015-8480-7.

Wessem, J.M. van, W.J. van de Berg, B.P.Y. Noël, E. van Meijgaard, C. Amory, G. Birnbaum, C.L. Jakobs, K. Krüger, J.T.M. Lenaerts, S. Lhermitte, S.R.M. Ligtenberg, B. Medley, C.H. Reijmer, K. van Tricht, L.D. Trusel, L.H. van Ulft, B. Wouters, J. Wuite, and M.R. van den Broeke (2018). "Modelling the climate and surface mass balance of

polar ice sheets using RACMO2 – Part 2: Antarctica (1979–2016)". In: *The Cryosphere* 12.4, pp. 1479–1498. ISSN: 1994-0424. DOI: 10.5194/tc-12-1479-2018.

Willen, M.O., M. Horwath, A. Groh, V. Helm, B. Uebbing, and J. Kusche (2022). "Feasibility of a global inversion for spatially resolved glacial isostatic adjustment and ice sheet mass changes proven in simulation experiments". In: *J. Geod.* 96.10, pp. 1–21. ISSN: 0949-7714. DOI: 10.1007/s00190-022-01651-8.

Willen, M.O., M. Horwath, L. Schröder, A. Groh, S.R.M. Ligtenberg, P. Kuipers Munneke, and M.R. van den Broeke (2020). "Sensitivity of inverse glacial isostatic adjustment estimates over Antarctica". In: *The Cryosphere* 14.1, pp. 349–366. DOI: 10.5194/tc-14-349-2020.